Communication

A First-Principles Study on the Reaction Mechanisms of Electrochemical CO_2 Reduction to C_1 and C_2 Products on Cu(110)

Yangyang Xu * and Lixin Zhang

School of Physics, Nankai University, Tianjin 300071, China; lxzhang@nankai.edu.cn
* Correspondence: 13516185067@163.com

Abstract: The mechanism of the electrochemical CO_2 reduction reaction on a Cu(110) surface has yet to be fully revealed. In this work, based on first-principles calculations, we investigate the mechanisms of the CO_2 reduction reaction to produce C_1 (including one C atom) and C_2 (including two C atoms) products on a Cu(110) surface. The results show that CH_4 and C_2H_5OH are the main C_1 and C_2 products on the Cu(110) surface, respectively. CH_4 is produced along the pathway $CO_2 \rightarrow COOH^* \rightarrow CO^* \rightarrow CHO^* \rightarrow CH_2O^* \rightarrow CH_3O^* \rightarrow CH_4$. C_2H_5OH is produced via the C-C coupling pathway between CO^* and CH_2O^* intermediates, which is the key reaction step. This is because CO^* and CH_2O^* coupling to CO-CH_2O^* has the lowest barrier among the CH_xO^* (x = 0–2) coupling pathways. Therefore, it is the most likely C-C coupling pathway. Further, CO-CH_2O^* is gradually hydrogenated to C_2H_5OH along the following pathway: CO-$CH_2O^* \rightarrow CHO$-$CH_2O^* \rightarrow CHOH$-$CH_2^* \rightarrow CH_2OH$-$CH_2^* \rightarrow CH_2OH$-$CH_3^* \rightarrow C_2H_5OH$.

Keywords: CO_2 reduction; C-C coupling; DFT; Cu(110) surface

1. Introduction

With the increase in the atmospheric CO_2 concentration, the global climate has undergone tremendous changes, such as global warming and ocean acidification [1,2]. Khalil et al. predicted that anthropogenic CO_2 levels will reach ~590 ppm in 2100, resulting in a global temperature increase of 1.9 °C [3]. In particular, the temperature increase in the polar regions will be up to three times as much as other regions [4]. These changes have seriously harmed the environment in which human beings live. The Paris Agreement adopted by the Intergovernmental Panel on Climate Change (IPCC) aims to reduce net levels of CO_2 in the atmosphere by 2050 [5]. To solve this problem, CO_2 capture and utilization, conversion and utilization, have become focuses of research [6,7]. Due to the disadvantages of CO_2 capture and utilization, such as CO_2 gas leakage and complex design, its large-scale popularization has limitations. However, CO_2 conversion and utilization has significant advantages. Photocatalysis [8], photo-electrocatalysis [9], and electrocatalysis [10] techniques have been widely used for CO_2 conversion and utilization. These techniques can not only reduce the concentration of CO_2 in the atmosphere, but also convert CO_2 into chemicals. Therefore, they have been widely concentrated on by researchers.

Photocatalysis and photo-electrocatalysis techniques refer to the conversion of solar energy into chemical energy [11,12]. They are carried out in an electrolytic cell, which includes two components (i.e., anode and cathode). On the cathode side, CO_2 reduction takes place on a p-type semiconductor, such as Cu_2O or TiO_2; on the anode side, water oxidation occurs on an n-type semiconductor such as F_2O_3. Semiconductor materials have been applied to photocatalysis and photo-electrocatalysis in CO_2 reduction reactions [13]. Their electronic structures play vital roles in photochemical and photoelectrochemical processes. The semiconductor materials are composed of a filled valence band (VB) coupled with an empty conduction band (CB), which shows an electron transfer from the VB to CB under stimulation by photons. The electron transfer leads to a positive hole in the VB.

These holes and the electrons formed on the surface of semiconductor materials can reduce the adsorbed species in the semiconductor materials [14]. The suitable electrode material can reduce the activation energy of a CO_2 reduction reaction, especially CO_2 reduction to C_2 products. The reason is that the electrode material can form $C_2O_2^{\bullet-}$, a transition state complex, by transferring electrons in the C-C coupling process. The electrons in the d orbital of the electrode are transferred to the π^* antibonding orbital of the $C_2O_2^{\bullet-}$ intermediate, which stabilizes the $C_2O_2^{\bullet-}$ intermediate adsorbed on the electrode surface, thus allowing the band bending reaction and reducing the activation energy of the C-C coupling process to promote the production of C_2 products [15]. Although metal oxides are commonly used to study photocatalysis [16,17] and photo-electrocatalysis, their inherent properties affect the catalytic efficiency to a certain extent. For example, the wide bandgap of TiO_2 (3.2 eV) leads to low photocatalytic efficiency owing to the very limited absorption of the solar spectrum [18]; due to the self-reduction potential between CB and VB energy values, Cu_2O in an aqueous solution has serious photocorrosion, resulting in the decrease in photocurrent density and the decrease in solar-fuel conversion efficiency [19].

To overcome this defect, various strategies have been proposed in recent years such as band gap engineering or surface coating, which can improve the catalytic efficiency of semiconductors. However, there are also some problems: it is a challenge to reduce the bandgap of TiO_2 while maintaining sufficient redox potentials at the band edge positions for a CO_2 reduction reaction; the use of a surface coating strategy to solve the photocorrosion of Cu_2O while maintaining its long-term stability is also a challenge.

Not only that, plasmonic materials are developed by researchers as photocatalysts. For the first time, Tirumala et al. have experimentally demonstrated that dielectric Mie resonance can significantly enhance photocatalysis in semiconductor materials when illuminated by visible light. These materials, characterized by their positive permittivity and moderate to high refractive indices, represent a groundbreaking advancement in the field [20,21]. Plasmonic materials with nanostructures can focus light at the nanoscale [22]. Under illumination, surface plasma excitation is established when the frequency of the incident light matches the natural frequency of oscillating surface electrons on a plasma with nanostructures. The redistributing light field, excited carriers, and heat effects produced during the relaxation process of the surface plasmon can set the stage for activating the CO_2 molecule. These excited carriers (hot electrons and holes) can offer opportunities for a CO_2 reduction reaction. By adjusting the size of the plasmonic materials, the absorption of a particular wavelength of sunlight can be realized to excite more carriers [23]. Generally speaking, the UV-Vis spectroscopy can be used as an in-line process analytical technology (PAT) tool for the operando characterization of nanostructures of plasmonic materials to trace the change in size of nanostructures [24]. Nonetheless, the short lifetime of excited carriers is the main factor restricting the application of plasma photocatalysts.

Compared to other techniques, the electrocatalysis technique is more easy due to the simple operating device and controllable reaction conditions. So, it is favored by researchers. It can convert CO_2 into a variety of value-added chemicals, including C_1 products such as methane (CH_4), formic acid (HCOOH), carbon monoxide (CO), and methanol (CH_3OH); C_2 products, such as ethylene (C_2H_4), ethanol (C_2H_5OH), and acetic acid (CH_3COOH); and C_3 products, such as propylene (C_3H_6) and propanol (C_3H_8O) [25–30]. Among them, C_2 products have higher energy density than C_1 products and are important raw materials in chemical synthesis [31–35]. In addition, the selective synthesis of C_2 products involves the formation of the C-C bond, namely, C-C coupling, which is a key challenge in heterogeneous catalysis during CO_2 reduction reactions [36,37]. Therefore, the electrocatalytic reduction of CO_2 to C_2 products has attracted wide attention, especially in identifying the reaction mechanism of this process.

Transition metals are often used as catalysts for CO_2 reduction reactions, especially the metal Cu. Compared with transition metals that produce hydrogenation, such as Pd [38], Fe [39] and others, Cu tends to reduce CO_2 to hydrocarbons. Moreover, Cu is a unique catalyst with selectivity for C_2 products during CO_2 reduction reactions. For example, it

has been shown in experiment that both Cu(100) and Cu(110) surfaces have high Faraday efficiency for C_2 products [40–42]. However, the CO_2 reduction products on Cu(100) and Cu(110) surfaces are different. In experiment, the Cu(100) surface mainly produces C_2H_4 [43], while the Cu(110) surface tends to produce C_2H_5OH and CH_3CHO [44]. The possible reason for this difference is that the coordination numbers of Cu(100) and Cu(110) surfaces are different. Compared to the Cu (100) surface, the Cu (110) surface has a lower coordination number. Therefore, the Cu (110) surface exhibits higher catalytic activity during the process of CO_2 reduction to C_2 products [45]. In theory, previous studies on the reaction mechanism of C_2 products mostly focused on the Cu(100) surface; however, few studies have focused on the Cu(110) surface [46,47]. Therefore, it is necessary to systematically study the reaction mechanism of C_2 product production on a Cu(110) surface.

Currently, the study of the CO_2 reduction reaction on a Cu(110) surface has been reported. In theory, Zhang et al. reported that CH_3OH is the main C_1 product on a Cu(110) surface and that CO^* and CH_2^* coupling to $CO\text{-}CH_2^*$ is the key to forming C_{2+} products [48]. Kuo et al. showed that CO^* and CH^* are high-concentration C_1 intermediates during the CO_2 electrochemical reduction to CH_4 on a Cu(110) surface. These are the possible C-C coupling species for C_{2+} product formation [49]. Bagger et al. showed that acetaldehyde is the main C_2 product on Cu(110) surfaces in theory [50]. In experiment, CH_3COOH is the main C_2 product reported by Takahashi et al. [51]. It remains challenging to reveal the main C_1 and C_2 products and the C-C coupling pathway for the CO_2 reduction reaction on a Cu(110) surface. What is clear, however, is that the two intermediates in which C-C coupling occurs form relatively easier in the C_1 product pathway.

Based on first-principles calculations, we propose that CH_4 and C_2H_5OH are the main C_1 and C_2 products on the Cu(110) surface, respectively, during the electrocatalytic reduction of CO_2. For CO_2 reduction to CH_4, we find this reaction along the following pathway: $CO_2 \rightarrow COOH^* \rightarrow CO^* \rightarrow CHO^* \rightarrow CH_2O^* \rightarrow CH_3O^* \rightarrow CH_4$. For reduction to C_2H_5OH, a C-C coupling pathway is required, which is a crucial reaction step. The energy barriers of C-C coupling among CH_xO^* (x = 0–2) are systematically compared. The results show that the CO^* and CH_2O^* coupling to $CO\text{-}CH_2O^*$ is the most likely C-C coupling pathway with the lowest energy barrier. Then, C_2H_5OH is produced along the following pathway: $CO\text{-}CH_2O^* \rightarrow CHO\text{-}CH_2O^* \rightarrow CHOH\text{-}CH_2^* \rightarrow CH_2OH\text{-}CH_2^* \rightarrow CH_2OH\text{-}CH_3^* \rightarrow C_2H_5OH$. This study provides theoretical guidance for further investigating more C_{2+} products on a Cu(110) surface.

2. Results and Discussion

2.1. CO₂ Reduction to CH₄

The Gibbs free energies of the reduction of CO_2 into CH_4 are calculated, and the results are shown in Figure 1. All of the intermediates are adsorbed on the most favorable sites, and their optimized adsorption geometries are shown in the insets. In addition, the bond distances between intermediates and Cu(110) surface are shown in Figure S1 of the Supplementary Materials. It is worth noting that we only label the key intermediates in the figures in this study. In addition, the solvent molecule has been removed from the figures to clearly show the adsorption geometries.

Our calculations show the reduction of CO_2 to CH_4 along the COOH pathway on the Cu(110) surface. Previous studies have indicated that the Cu(110) surface with a coordination number of seven tends to follow the COOH pathway. In contrast, the Cu(111) surface with a coordination number of nine prefers to follow the HCOO pathway [52,53]. This also proves that our calculation results can be trusted.

In Figure 1, the potential−limiting step is the formation of a $COOH^*$ intermediate on the Cu(110) surface. Because this step has the highest positive variation of Gibbs free energy of 0.66 eV among all reaction steps from CO_2 reduction to CH_4. Our result is close to the ΔG(0.76 eV) for forming $COOH^*$ on Cu(110) in the previous literature [54]. Since our calculations take into account the solvent effect, the ΔG of forming $COOH^*$ on the Cu(110) surface is lower. An earlier report also suggests that the formation of $COOH^*$ is

the potential-determining step on the Cu(110) surface [55], which is consistent with our calculation. For the step of COOH* → CO*, COOH* binds with H to form CO* and $H_2O(g)$. Since CO* is the important intermediate that participates in the CO_2 reduction reaction, we only label it in Figure 1.
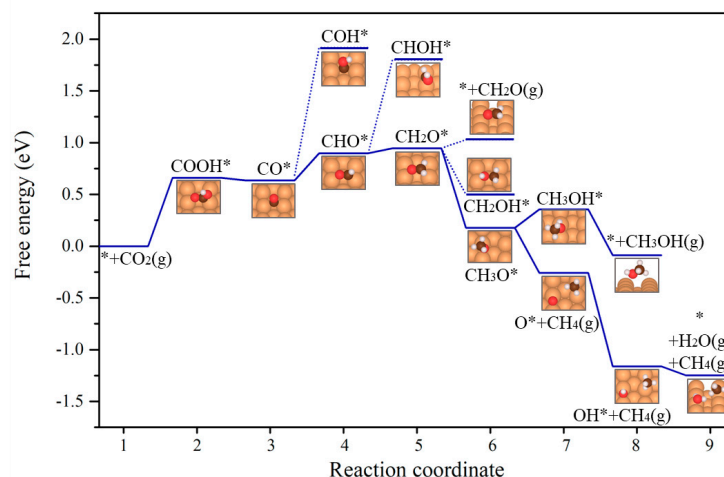

Figure 1. Gibbs free energy diagram for CO_2 reduction to CH_4 on the Cu(110) surface. The energy of [* + $CO_2(g)$ + $4H_2(g)$] is set as a reference. X* represents species X adsorbed on the Cu(110) surface. The optimized adsorption geometries of key intermediates are shown in the insets. Cu: yellow, C: brown, O: red, H: white.

For the CO*, it may involve either desorption or hydrogenation on the Cu(110) surface. To compare which is the next possible reaction of CO*, the activation energies of CO* desorption and hydrogenation are calculated, and the results are shown in Figure S2 of the Supplementary Materials and Figure 2, respectively. The activation energy of CO* desorption is 1.31 eV; the activation energies of CO* hydrogenation to CHO* and COH*are 1.10 and 2.56 eV, respectively. Although the activation energy of CO* desorption is higher than that of the hydrogenation to COH*, it is lower than that of hydrogenation to CHO*. Therefore, CO* prefers hydrogenation rather than desorption on a Cu(110) surface.

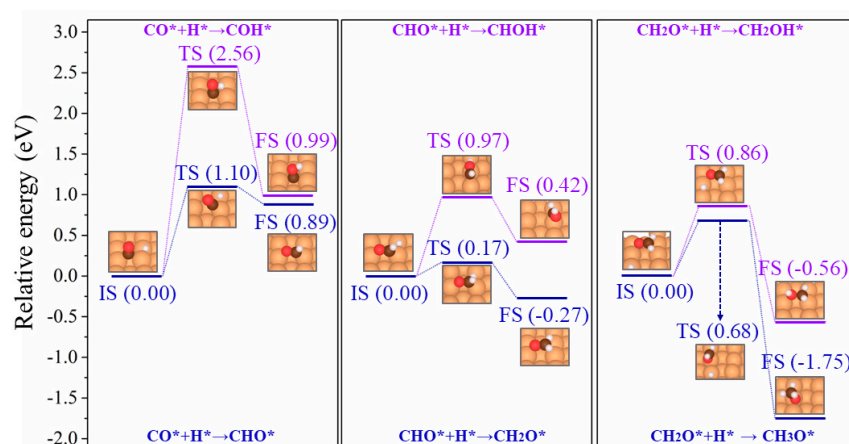**Figure 2.** A schematic potential energy diagram from CO* hydrogenation to CH_3O* on the Cu(110) surface. The optimized adsorption geometries of the initial states, transition states, and finial states are shown in the insets. Cu: yellow, C: brown, O: red, H: white.

For the hydrogenation of CO*, we find that H prefers to bond with C atoms of intermediates rather than O atoms. For example, for the steps of CO* → COH* and CO* → CHO*, the reaction energies are 1.28 and 0.26 eV, respectively. For the steps of CHO* →

CHOH* and CHO* → CH$_2$O*, the reaction energies are 0.90 and 0.05 eV, respectively. For the steps of CH$_2$O* → CH$_2$OH* and CH$_2$O* → CH$_3$O*, the reaction energies are 0.08 and −0.77 eV, respectively. Obviously, for the steps from CO* to CH$_3$O*, the reaction energies of the H bonding with the C atom of intermediates are at least 0.80 eV lower than that of O atom bonding. Therefore, CO* hydrogenation to CH$_3$O* occurs along the following pathway: CO* → CHO* → CH$_2$O* → CH$_3$O*. Then, the H bonds with the O atom of the CH$_3$O* intermediate to produce CH$_4$. This is the most likely pathway for the formation of a surface treated by ultrapure water treatment in the experiment in the CO$_2$ reduction reaction [51].

2.2. The Activation Energies from CO* Hydrogenation to CH$_x$O*

To verify the accuracy of our results, we also calculate the activation energies of steps from CO* to CH$_3$O*, which are shown in Figure 2. The bond distances of the initial states, transition states, and finial states between them and the Cu(110) surface are shown in Figure S3 of the Supplementary Materials. The E_a of steps from CO* to COH* and CHO* are 2.57 and 1.10 eV, respectively. The E_a of steps from CHO* to CHOH* and CH$_2$O* are 0.97 and 0.17 eV, respectively. The E_a of steps from CH$_2$O* to CH$_2$OH* and CH$_3$O* are 0.86 and 0.68 eV, respectively. Obviously, the activation energies of steps from CO* to CHO*, CH$_2$O*, and CH$_3$O* are lower than those from CO* to COH*, CHOH*, and CH$_2$OH*, respectively. This indicates that CO* hydrogenation to CH$_3$O* prefers to be along the following pathway: CO* → CHO* → CH$_2$O* → CH$_3$O*. Given our analysis above, we can conclude that CO$_2$ reduction to CH$_4$ along the following pathway: CO$_2$ → COOH* → CO* → CHO* → CH$_2$O* → CH$_3$O* → CH$_4$.

The step of CO* + H* → CHO* has relative high activation energy among the efficient pathway of the hydrogenation of CO* to CH$_3$O*, i.e., the steps of CO* + H* → CHO*, CHO* + H* → CH$_2$O*, and CH$_2$O* + H* → CH$_3$O*. In addition to forming COOH*, this could possibly be the other potential bottleneck in the reaction of CO$_2$ reduction to CH$_4$. To eliminate this potential bottleneck, applying tensile strain on a Cu(110) surface is an effective strategy. Shin et al. designed a novel catalyst that uses silver (Ag) and palladium (Pd) to support Cu thin film to decrease the activation energy of steps of CO* + H* → CHO* [56]. This provides a new way for us to design new catalysts.

By comparing the activation energies for the steps from CO* to CH$_3$O*, we can not only prove the effectiveness of generating the CH$_4$ pathway, but also identify the intermediates enriched on the Cu(110) surface. These intermediates are prone to C-C coupling. So, comparing the activation energies for the steps from CO* to CH$_3$O* can provide guidance for the study of a possible C-C coupling pathway. Thus, we believe that comparing the activation energies for the steps from CO* to CH$_3$O* can influence the pathway of C-C coupling.

2.3. C-C Coupling Pathway

In exploring the pathway of CO$_2$ reduction to CH$_4$, we find that CHO* and CH$_2$O* formed by CO* hydrogenation tend to be enriched on the Cu(110) surface. The main reason for this is that compared with other reaction steps, the steps of CO* → CHO* and CO* → CH$_2$O* have relatively lower activation energies. Moreover, the step of CH$_2$O* → CH$_3$O* requires slightly high activation energy so that CH$_2$O* prefers to remain on the Cu(110) surface. Therefore, we believe that CHO* and CH$_2$O* tend to be enriched on the Cu(110) surface for the C-C coupling. In addition, we also consider CO* for the C-C coupling intermediate. Not only is it a common intermediate in C-C coupling, but its coupling with another CO* is also widely studied on low-index Cu surfaces [57].

We believe that C-C coupling will likely occur between CO*, CHO*, and CH$_2$O*, labeled CH$_x$O* (x = 0–2). The six pathways of C-C coupling are explored: (a) two-CO* dimerization; (b) CO* and CHO* coupling; (c) CO* and CH$_2$O* coupling; (d) CHO* and CH$_2$O* coupling; (e) CHO* and CHO* coupling; and (f) CH$_2$O* and CH$_2$O* coupling.

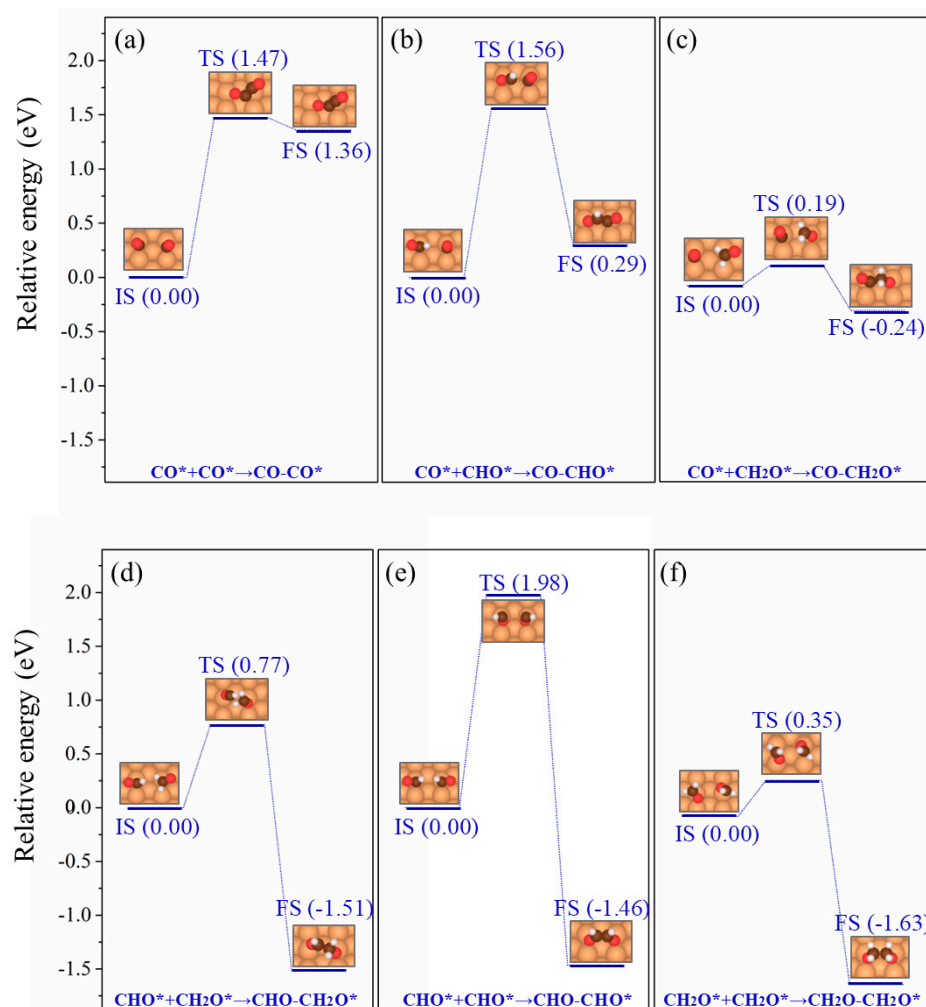We calculate the Gibbs free energies for these six pathways, and the results are shown in Figure 3.

Figure 3. Schematic potential energy diagrams for (**a**) two-CO* dimerization, (**b**) CO* and CHO* coupling, (**c**) CO* and CH₂O* coupling, (**d**) CHO* and CH₂O* coupling, (**e**) CHO* and CHO* coupling, and (**f**) CH₂O* and CH₂O* coupling on the Cu(110) surface. The optimized adsorption geometries of initial states, transition states, and finial states are shown in the insets. Cu: yellow, C: brown, O: red, H: white.

It is worth noting that the intermediates of C-C coupling refer to intermediates that are co-adsorbed on a Cu(110) surface. The two-CO* dimerization pathway refers to the coupling between one CO* and another CO* that are co-adsorbed on a Cu(110) surface. The CO* and CHO* coupling pathway refers to the coupling of one CO* and one co-adsorbed CHO*. For this pathway, besides the reaction step of CO* and CHO* coupling being endothermic, the formation of CHO* is also endothermic. That is to say, in addition to the energy barrier required for C-C coupling to occur, it is also necessary to consider the energy barrier required to form C-C coupling intermediates.

In this case, the two-CO* dimerization pathway need overcome the energy barrier of C-C coupling with 1.47 eV. However, the CO* and CHO* coupling pathway is required to overcome an energy barrier of 2.66 eV. This includes two parts: one is from CO* to CHO*, with 1.10 eV; the other is from CO* and CHO* coupling, with 1.56 eV. Comparing these two C-C coupling pathways, the two-CO* dimerization is more likely to occur because it requires overcoming a lower energy barrier.

Similar situations also occur in other C-C coupling pathways. For the CO* and CH$_2$O* coupling pathway, the energy barrier to be overcome is 1.46 eV. This also includes two parts: one is from CO* to CH$_2$O*, with 1.27 eV; the other is from CO* and CH$_2$O* coupling, with 0.19 eV. For the CHO* and CH$_2$O* coupling pathway, the energy barrier to be overcome is 3.14 eV. This includes three parts: one is from CO* to CHO*, with 1.10 eV; one is from the other CO* to CH$_2$O*, with 1.27 eV; the last is CHO* and CH$_2$O* coupling, with 0.77 eV. For the CHO* and CHO* coupling pathway, the energy barrier to be overcome is 4.18 eV. This includes three parts: one is from CO* to CHO*, with 1.10 eV; one is from the other CO* to CHO*, with 1.10 eV; the last one is CHO* and CHO* coupling, with 1.98 eV. For the CH$_2$O* and CH$_2$O* coupling pathway, the energy barrier to be overcome is 2.89 eV. It includes three parts: one is from CO* to CH$_2$O*, with 1.27 eV; one is from the other CO* to CH$_2$O*, with 1.27 eV; the last one is CH$_2$O* and CH$_2$O* coupling, with 0.35 eV. By comparing the energy barriers of these six C-C coupling pathways, we find that the energy barrier of CO* and CH$_2$O* coupling to form CO-CH$_2$O * is the lowest with 1.46 eV.

It is worth noting that the two-CO* dimerization pathway (1.47 eV) has a similar energy barrier with coupling of CO* and CH$_2$O* (1.46 eV). To compare which of these two C-C coupling pathways is the most likely, the adsorption energies of CO-CO* and CO-CH$_2$O* intermediates are calculated to evaluate the adsorption strengths of them on a Cu(110) surface. The E_{ads} of the CO-CO* intermediate is -1.93 eV; the E_{ads} of the CO-CH$_2$O* intermediate is -0.28 eV. Obviously, the adsorption energy of the CO-CH$_2$O* intermediate on a Cu(110) surface is more positive. This indicates that the adsorption strength of the CO-CH$_2$O* intermediate to Cu(110) is stronger. It will make the CO-CH$_2$O* intermediate occupy more active sites, thus weakening the adsorption strength of CO-CO* on a Cu(110) surface. Therefore, even though two-CO* dimerization has a similar energy barrier to CO* and CH$_2$O* coupling, CO* and CH$_2$O* coupling is the most likely C-C coupling pathway on a Cu(110) surface.

As we know, the geometric and electronic structures of intermediates play significant roles in the process of C-C coupling. The density of states (DOSs) of six C-C coupling pathways are calculated. The result for the CO* and CH$_2$O* coupling pathway, i.e., the most likely C-C coupling pathway, is shown in Figure 4a. Other results of DOS for C-C coupling pathways are shown in Figure S4 of the Supplementary Materials.
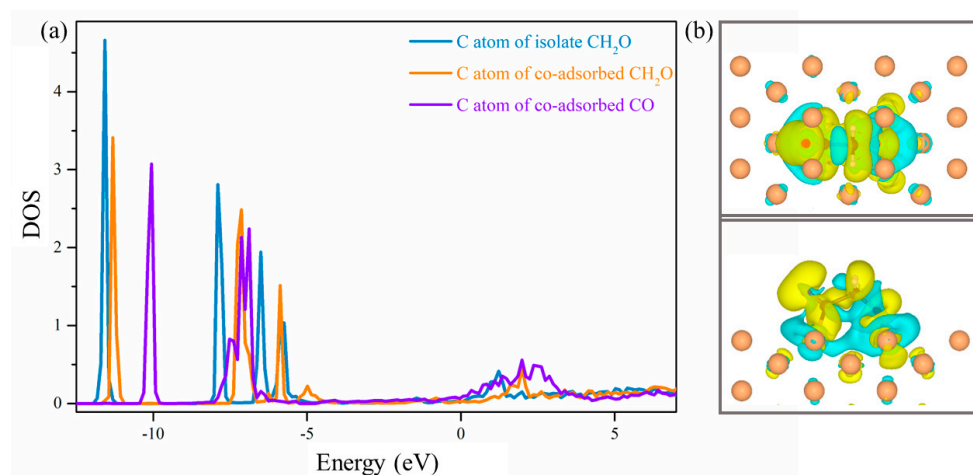

Figure 4. (**a**) The DOSs of C atoms in the adsorbed intermediates for the CO* and CH$_2$O* coupling pathway on the Cu(110) surface. (**b**) Diagrams of the difference in charge densities of CO-CH$_2$O* on the Cu(110) surface by an isosurface of 0.002 eV/Å. Yellow represents an electron-accumulation region and blue represents an electron-loss region. $\Delta\rho = \rho(X^*) - \rho(*) - \rho(X)$.

For the CO* and CH$_2$O* coupling pathway, the C atoms of CO* and CH$_2$O* are adsorbed on the Cu(110) surface, respectively. Compared with the DOS peak of the C atom in isolated CO*, the DOS peak of the C atom in co-adsorbed CO* on the Cu(110) surface

decreases; compared with the DOS peak of the C atom in isolated CH_2O^*, the DOS peak of the C atom in co-adsorbed CH_2O^* on the Cu(110) surface also decreases. So, compared with the isolate species on the Cu(110) surface, the DOS peaks of co-adsorbed CO^* and CH_2O^* distinctly change, as shown in Figure 4a. The reason for this is the orbital overlap of C atoms in co-adsorbed CO^* and CH_2O^*. This indicates a strong interaction between CO^* and CH_2O^*. Therefore, the CO^* and CH_2O^* coupling has a low activation energy.

For the two-CO^* dimerization pathway, although the DOS peaks of C atoms in the two CO^* are slightly low compared to that of the isolate CO^* on the Cu(110) surface, as shown in Figure S4a, the DOS peaks of C atoms in co-adsorbed CO^* on the Cu(110) surface are similar. This demonstrates that orbital overlap of the C atoms is very low in two $^*CO$ molecules, and thus there is weak interaction between co-adsorbed CO^*. So, the CO^* dimerization has a high activation energy. For the pathways of CHO^* and CHO^* coupling, CH_2O^* and CH_2O^* coupling, similar cases take place, as shown in Figure S4d and S4e, respectively. When C-C coupling occurs between the same two intermediates, the repulsion between them causes the distance between them to become larger. So, C atomic orbitals do not overlap significantly, which may be the main reason why the DOS peaks of the C atoms do not change significantly. For the CO^* and CHO^* coupling pathway, compared with the isolate CHO^* on the Cu(110) surface, the DOS peak of the C atom of co-adsorbed CHO^* is slightly changed, as shown in Figure S4b. That is to say, the interaction of co-adsorbed CHO^* and CO^* is weak. For CHO^* and CH_2O^* coupling, the DOS peak of the C atom in isolate CHO^* is similar to that of co-adsorbed CHO^*; the DOS peak of the C atom in isolate CH_2O^* is similar to that of co-adsorbed CH_2O^*. This indicates that the interaction between co-adsorbed CHO^* and CH_2O^* is weak. Therefore, given our analysis above, it can conclude that CO^* and CH_2O^* is the most likely C-C coupling pathway on the Cu(110) surface.

The previous literature suggested that CO^* and CH^* coupling is a possible C-C coupling pathway on a Cu(110) surface, and CH^* formation along the pathway $CO^* \rightarrow CHO^* \rightarrow CHOH^* \rightarrow CH^*$ [48]. In the literature, CHO^* tends to be hydrogenated to $CHOH^*$ adsorbed on a Cu(110) surface rather than $CH_2O(g)$ desorbed from the surface. It is worth noting that the adsorption of CH_2O^* on a Cu(110) surface is completely ignored. Besides the hydrogenation in CHO^* to $CHOH^*$ and $CH_2O(g)$ mentioned in the literature, the adsorbed $CH_2O(g)$ must also be considered. We calculated the reaction energy of the $CHO^* \rightarrow CH_2O^*$ step to compare with the $CHO^* \rightarrow CHOH^*$ step, and the results are shown in Figure 1. The result shows that, comparing the $CHO^* \rightarrow CHOH^*$ and $CHO^* \rightarrow CH_2O(g)$ steps, the reaction energy of the $CHO^* \rightarrow CH_2O^*$ step is the lowest. Thus, CHO^* prefers hydrogenation to CH_2O^* adsorbed on a Cu(110) surface rather than $CHOH^*$. Thus, the CH^* formed along the pathway $CHO^* \rightarrow CHOH^* \rightarrow CH^*$ is a challenge.

The differences in charge densities of C-C coupling intermediates are calculated and the results are shown in Figure 4b and Figure S5 in the Supplementary Materials, which have been widely used to analyze the interactions between an intermediate and catalyst surface and stability of intermediate on a Cu surface [58,59]. For six C-C coupling intermediates, the electron overlap area around Cu atoms is the most large when the $CO-CH_2O^*$ intermediate is adsorbed on the Cu(110) surface. It reveals that the interaction between the $CO-CH_2O^*$ intermediate and Cu(110) surface is the strongest among six C-C coupling intermediates. Because the stronger interaction between the intermediate and the Cu surface, the higher stability of intermediate. Thus, we believe that the $CO-CH_2O^*$ intermediate is the most stable on the Cu(110) surface. This supports that CO^* and CH_2O^* coupling is the most likely C-C coupling pathway.

Here, in addition to thermodynamics, other possible C-C coupling pathways do exist if the effects of other factors on C-C coupling are considered, especially the reconstruction of copper electrodes under real reaction conditions. However, further theoretical study may be needed to make an accurate evaluation.

2.4. C₂H₅OH Production Pathway

Now that we know that the CO^* and CH_2O^* coupling to $CO\text{-}CH_2O^*$ is the most likely C-C coupling pathway, we explore C_2 products from there. We calculate the Gibbs free energies to produce CH_3CH_2OH, i.e., C_2H_5OH, and the results are shown in Figure 5. In Figure 5, C_2H_5OH is produced along the following pathway: $CO\text{-}CH_2O^* \rightarrow CHO\text{-}CH_2O^*$ $\rightarrow CHOH\text{-}CH_2^* \rightarrow CH_2OH\text{-}CH_2^* \rightarrow CH_2OH\text{-}CH_3^* \rightarrow C_2H_5OH$. From $CO\text{-}CH_2O^* \rightarrow$ $CH_2OH\text{-}CH_3$, only the reaction steps of $CO\text{-}CH_2O^* \rightarrow CHO\text{-}CH_2O^*$ and $CHOH\text{-}CH_2^* \rightarrow$ $CH_2OH\text{-}CH_2^*$ are slightly endothermic. This indicates that the process of C_2H_5OH production from $CO\text{-}CH_2O^*$ can easily take place. This is also consistent with the observation in experiment that the oxygenated hydrocarbon products are the main products on a Cu(110) surface [44].
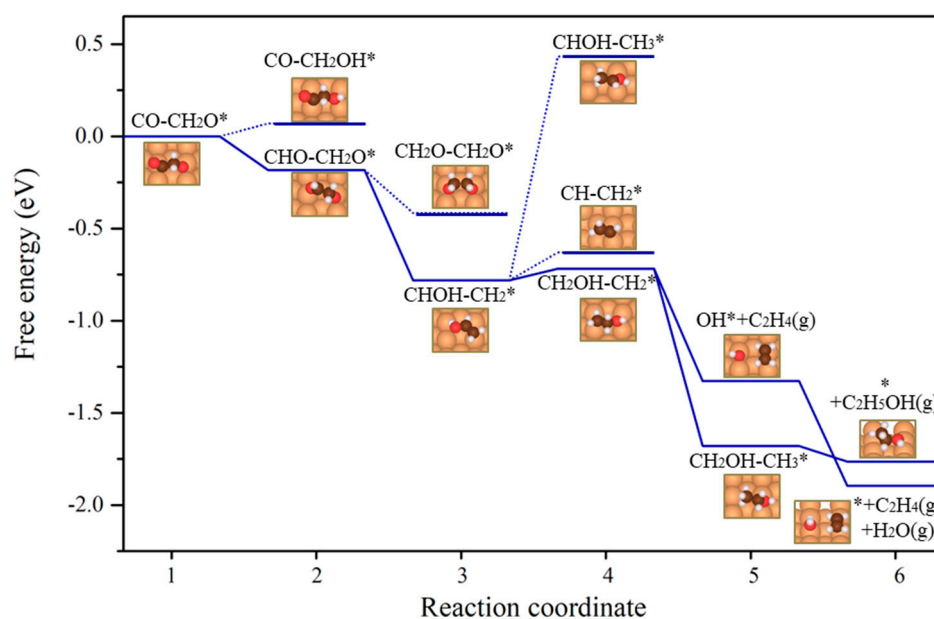

Figure 5. Gibbs free energy diagram for the production of C_2H_5OH on the Cu(110) surface. The optimized adsorption geometries of key intermediates are shown in the insets. Cu: yellow, C: brown, O: red, H: white.

It is worth noting that the hydrogenation of $CH_2OH\text{-}CH_2^*$ is the key to determining the product selectivity on a Cu(110) surface. The reaction energy of the $CH_2OH\text{-}CH_2^* \rightarrow$ $CH_2OH\text{-}CH_3^*$ step is -1.65 eV; the $CH_2OH\text{-}CH_2^* \rightarrow OH^* + C_2H_4(g)$ step is -1.42 eV. It is obvious that the reaction energy of the $CH_2OH\text{-}CH_2^* \rightarrow CH_2OH\text{-}CH_3^*$ step is lower. Thus, we believe that the $CH_2OH\text{-}CH_2^*$ is prone to hydrogenation to $CH_2OH\text{-}CH_3^*$, which then desorbs from the Cu(110) surface to produce C_2H_5OH. Although it has been indicated that $CHO\text{-}CH_2$ is the key to determine the product selectivity of a Cu catalyst, the surface morphology or crystal orientation of a Cu catalyst is not indicated [60]. Additionally, the previous literature indicated that the carbon monoxide initially dimerizes and is protonated to form $^*(OH)C{=}COH$ on Cu(100) [61]. However, the calculation of activation energy shows that COH^* is difficult to form on a Cu(110) surface, so we believe that the $^*(OH)C{=}COH$ is not likely to occur on a Cu(110) surface.

By comparing the reaction energy of the possible formation intermediates, we identify the intermediates with smaller reaction energy. So, the reaction mechanisms of generating CH_4 and C_2H_5OH are revealed. In other words, even if the coverage scenario of the same intermediate is increased, the reaction mechanism is still not affected. Therefore, for the same intermediate, increasing the coverage scenario can reduce the hydrogenation reaction or C-C coupling reaction energy and improve the product efficiency, but does not affect the reaction mechanism.

2.5. The Analysis of Applied Potential

Our conclusion above is obtained at a zero applied potential, representing the reaction when no external potential is applied. The applied potential is the minimum required potential on which all elementary reaction steps become exergonic [62]. Therefore, the required applied potential is the potential of the potential-limiting step. We compared the production of CH_4 and C_2H_5OH based on the applied potential in this section. For the reduction of CO_2 to CH_4 and C_2H_5OH, the potential-limiting steps are the formation of COOH* with 0.66 eV. Obviously, the applied potential with -0.66 V (vs. RHE) is required to eliminate the energy barrier. The negative sign indicates a reduction reaction. The Gibbs free energies of CO_2 reduction to CH_4 and C_2H_5OH with an applied potential of -0.66 V (vs. RHE) are calculated, and the results are shown in Figure 6. It is worth noting that even if the applied potentials are the same for CH_4 and C_2H_5OH production, the Cu(110) surface prefers to produce C_2H_5OH. The main reason is that the Cu(110) surface is unstable under CO_2 reduction reaction conditions. This allows the morphology of the Cu(110) surface to evolve into a complex topography of the active site, which is favorable for the formation of C_2 products [63].
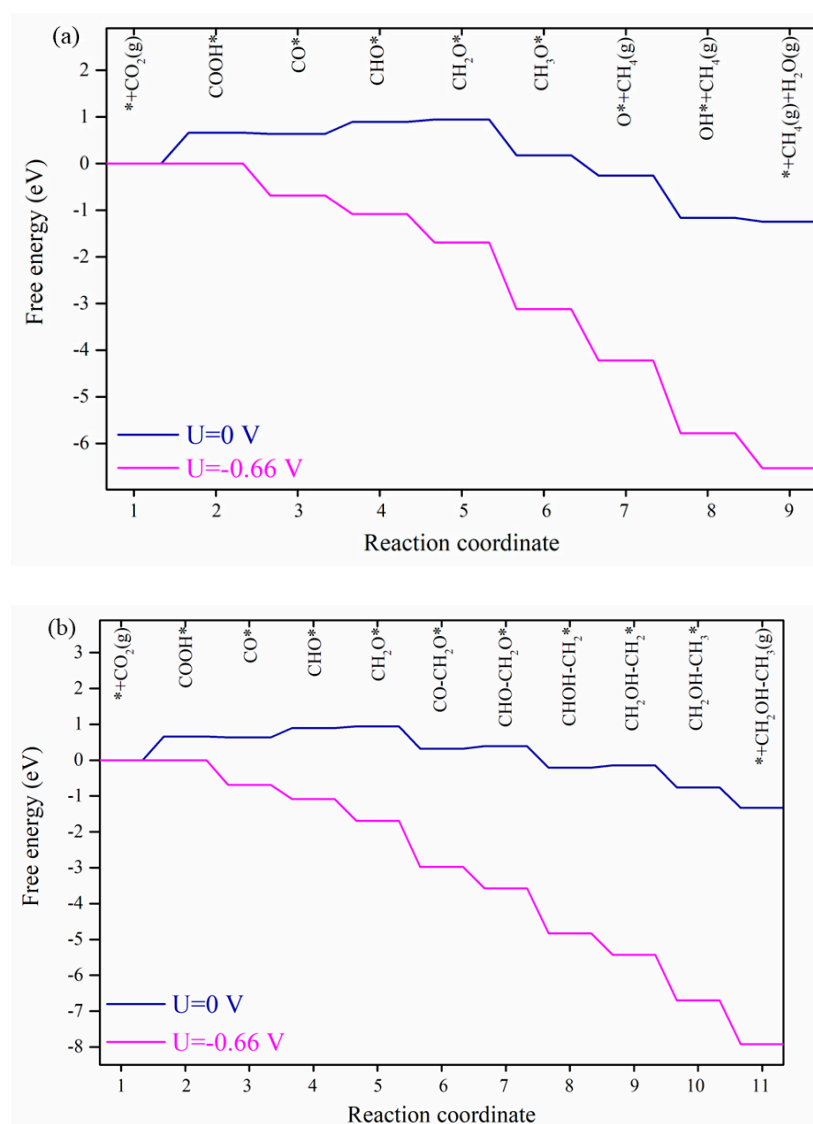

Figure 6. Gibbs free energy diagrams for CO_2 reduction to (**a**) CH_4 and (**b**) C_2H_5OH on Cu(110) surface with applied potentials of 0 V and -0.66 V versus RHE.

In addition, the Gibbs free energies of CO_2 reduction to CH_3OH and C_2H_4 with an applied potential of -0.66 V (vs. RHE) are also calculated, and the results are shown in Figure S6 of the Supplementary Materials. For CO_2 reduction to CH_3OH, the steps (* + CO_2(g)$\rightarrow$ COOH* and CH_3O^* $\rightarrow$ CH_3OH^*) are a positive variation of Gibbs free energies. Thus, the step of * + CO_2(g)$\rightarrow$ COOH* is the potential-limiting step for CH_3OH production, which is consistent with CH_4 production. Thus, the applied potential of CO_2 reduction to CH_4 and CH_3OH is the same. A similar situation occurs in CO_2 reduction to C_2H_4. Although C-C coupling is an important reaction step, the step of * + CO_2(g)$\rightarrow$ COOH* is the potential-limiting step for C_2H_4 and C_2H_5OH production.

3. Computation Details

The calculations are performed within the framework of density functional theory as implemented in the Vienna Ab initio Simulation Package (VASP) [64,65]. The Kohn–Sham wave functions are expanded in a plane wave basis set with a cut-off energy of 550 eV. The projector-augmented wave (PAW) method and Perdew–Burke–Ernzerhof (PBE) potential for the exchange–correlation function are used [66]. Eleven-layer slab model with a surface periodicity of 3×5 is used to describe the Cu(110) surface, as shown in Figure 7. The two bottommost layers of the model system are fixed to the optimized bulk parameters, and the rest are fully relaxed during geometry optimization. The convergence criteria for energy and force are set to 1×10^{-4} eV and 0.01 eV/Å, respectively. The thickness of the vacuum layer is ~15 Å, which is set to avoid interaction between slabs. The Monkhorst–Pack k-point mesh is $2 \times 2 \times 1$. The calculated lattice constant of Cu is 3.61 Å [67], which agrees with the experimental value of 3.62 Å [68,69]. Dipole corrections are applied. We use an empirical dispersion correction (D3) for the van der Waals contributions [70]. The transition state (TS) is obtained using the climbing-image nudged elastic band (CI-NEB) method [71] by using 5 images, including the initial and final states, during the transition state search. This is verified by obtaining only one imaginary frequency at each TS configuration [72,73]. In this study, we only analyze the thermodynamic trend of the CO_2 reduction reaction according to the transition states reported in [74]. Additional computational details are provided in the Supplementary Information.
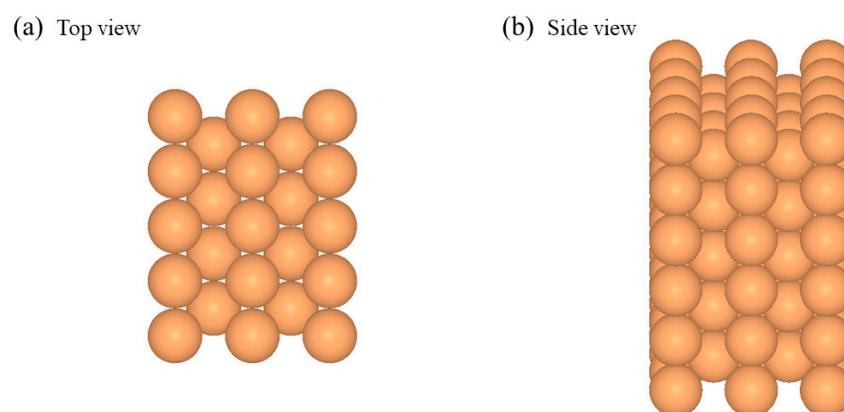
(**a**) Top view　　　　　　　　　　　(**b**) Side view

Figure 7. The (**a**) top view and (**b**) side views of the Cu(110) surface. Cu: yellow.

The Gibbs free energy of each elementary step is defined as

$$\Delta G = \Delta E + \Delta E_{ZPE} - T\Delta S \qquad (1)$$

where ΔE is the reaction energy of each elementary step calculated from DFT total energies. ΔE_{ZPE} and ΔS are the zero point energy (*ZPE*) difference and the reaction entropy change

between the two states of the reaction step. In this work, the temperature is 298.15 K and pressure is 1 atm. E_{ZPE} is expressed as the following equation:

$$E_{ZPE} = \sum_i \frac{1}{2} h v_i \tag{2}$$

where vibrational frequency (v_i) is calculated using a method from [75], and only the surface-adsorbed species are allowed to shift during the calculation.

The adsorption energy (E_{ads}) of an intermediate on Cu(110) is defined as

$$E_{ads} = E_* + E_X - E_{X^*} \tag{3}$$

where E_{X^*} and E_* are the total energies of the surfaces with and without the adsorbed intermediates. The E_X is the energy of an intermediate, which can be defined as the sum of E_C, E_O, and E_H of the intermediate. The E_C, E_O, and E_H are referenced to the energies of CO_2, H_2, and the difference between H_2O and H_2, respectively. By this definition, more positive E_{ads} means stronger binding. Our calculation method is consistent with that of Dong et al. [76].

The step with the highest positive variation of Gibbs free energy is the potential-limiting step. During an external applied potential (U) in the reaction, the chemical potential of each elementary step changes by eU. e is the electronic charge transferred in each elementary step. The relative energy is obtained by the Gibbs free energy difference between the initial state and the final state of each elementary step [77,78]. The activation energy (E_a) of the reaction step is defined as

$$E_a = E_{TS} - E_{IS} \tag{4}$$

where E_{TS} and E_{IS} are the energy of the transition state and initial state of the reaction step. The proton–electron pairs during the CO_2 reduction reaction can be written as follows [79]:

$$H^+ + e^- \rightarrow \frac{1}{2} H_{2(g)} \tag{5}$$

where the chemical potential of proton–electron pairs can be treated as half the energy of hydrogen.

Since the CO_2 reduction reaction occurs in a solvated environment, we only consider a single solvent water molecule to reduce the cost of calculation. Thus, an explicit water molecule is included in the computational model to account for the role of solvation. Although the solvation effect can be represented in terms of a single water molecule, it can be inaccurate and lead to errors. However, Luo et al. reported that even if a full solvation model is considered during the CO_2 reduction reaction on low-index Cu surfaces, the results are similar or slightly different from those of a single-water-molecule model. This also shows the rationality of our use of a single-water-molecule model [80].

4. Conclusions

In summary, based on first-principles calculations, we find that the C_1 and C_2 products of CO_2 reduction on a Cu(110) surface are CH_4 and C_2H_5OH, respectively. CH_4 is produced via the $CO_2 \rightarrow COOH^* \rightarrow CO^* \rightarrow CHO^* \rightarrow CH_2O^* \rightarrow CH_3O^* \rightarrow CH_4$ pathway. C_2H_5OH is produced through CO^* and CH_2O^* coupling to the $CO\text{-}CH_2O^*$ pathway. This is because this pathway has the lowest activation energy among the C-C coupling pathways between CH_xO^* (x = 0–2). Then, C_2H_5OH is produced along the following pathway: $CO\text{-}CH_2O^* \rightarrow CHO\text{-}CH_2O^* \rightarrow CHOH\text{-}CH_2^* \rightarrow CH_2OH\text{-}CH_2^* \rightarrow CH_2OH\text{-}CH_3^* \rightarrow C_2H_5OH$. Our results provide theoretical guidance for further understanding of the mechanism of C_2 production on a Cu(110) surface.

Supplementary Materials: The following supporting information can be downloaded at: https://www.mdpi.com/article/10.3390/catal14070468/s1, Figure S1: The optimized adsorption geometries of the intermediates in Figure 1 and the bonding distances between them and the Cu(110) surface are shown; Figure S2: Schematic potential energy diagram for CO* desorption from Cu(110) surface; Figure S3: The optimized adsorption geometries of initial states, transition states, and finial states involved in CO* reduction to CH_3O^* in Figure 2 and the bonding distances between them and the Cu(110) surface are also shown; Figure S4: Density of states (DOS) plots of C atoms of adsorbed intermediates in (a) two-CO*; (b) CO* and CHO*; (c) CHO* and CH_2O^*; (d) CHO* and CHO*; and (e) CH_2O^* and CH_2O^* pathways on Cu(110) surface; Figure S5: Diagrams of difference in charge densities of (a) CO-CO*; (b) CO-CHO*; (c) $CHO-CH_2O^*$; (d) CHO-CHO*; and (e) $CH_2O-CH_2O^*$ on Cu(110) surface; Figure S6: Gibbs free energy diagrams for CO_2 reduction to (a) CH_3OH and (b) C_2H_4 on the Cu(110) surface with applied potentials of 0 V and -0.66 V versus RHE. References [81–87] are cited in the supplementary materials.

References

1. Barberis, L.; Versteeg, C.I.; Meeldijk, J.D.; Stewart, J.A.; Vandegehuchte, B.D.; de Jongh, P.E. K and Na promotion enables high-pressure low-temperature reverse water gas shift over copper-based catalysts. *ACS Catal.* **2024**, *14*, 9188–9197. [CrossRef]
2. Zhong, C.Y.; Yang, Y.F.; Chen, J.; Feng, B.M.; Wang, H.B.; Yao, Y.X. Nickel nanoparticles supported on lanthanum oxycarbonate with interfacial oxygen vacancies as catalysts for CO_2 hydrogenation to methane. *ACS Appl. Nano Mater.* **2024**, *7*, 14057–14068. [CrossRef]
3. Khalil, M.; Gunlazuardi, J.; Ivandini, T.A.; Umar, A. Photocatalytic conversion of CO_2 using earth-abundant catalysts: A review on mechanism and catalytic performance. *Renew. Sustain. Energy Rev.* **2019**, *113*, 109246. [CrossRef]
4. Wu, H.L.; Li, X.B.; Tung, C.H.; Wu, L.Z. Semiconductor quantum dots: An emerging candidate for CO_2 photoreduction. *Adv. Mater.* **2019**, *31*, 1900709. [CrossRef] [PubMed]
5. Wei, Y.; Li, Y.; Wu, M.; Li, Y. The decomposition of total-factor CO_2 emission efficiency of 97 contracting countries in Paris Agreement. *Energy Econ.* **2019**, *78*, 365–378. [CrossRef]
6. Kar, S.; Goeppert, A.; Prakash, G.S. Combined CO_2 capture and hydrogenation to methanol: Amine immobilization enables easy recycling of active elements. *ChemSusChem* **2019**, *12*, 3172–3177. [CrossRef] [PubMed]
7. Yang, D.; Yu, H.; He, T.; Zuo, S.; Liu, X.; Yang, H.; Ni, B.; Li, H.; Gu, L.; Wang, D.; et al. Visible-light-switched electron transfer over single porphyrin-metal atom center for highly selective electroreduction of carbon dioxide. *Nat. Commun.* **2019**, *10*, 1–10. [CrossRef]
8. Liu, X.; Jing, X.C.; Liu, R.H.; Guo, P.Q.; Yin, Z.Y. Plasmon-enhanced perovskite photocatalysts for CO_2 reduction: A mini review. *Energy Fuels* **2024**, *38*, 4966–4979. [CrossRef]
9. Foster, B.M.; Paris, A.R.; Frick, J.J.; Blasini-Pérez, D.A.; Cava, R.J.; Bocarsly, A.B. Catalytic mismatching of $CuInSe_2$ and Ni_3Al demonstrates selective photoelectrochemical CO_2 reduction to methanol. *ACS Appl. Energy Mater.* **2020**, *3*, 109–113. [CrossRef]
10. Wang, X.; Mao, Y.; Wang, Z.Y. Plasmonic-assisted electrocatalysis for CO_2 reduction reaction. *ChemElectroChem* **2024**, *11*, e202300805. [CrossRef]
11. Han, G.H.; Bang, J.; Park, G.; Choe, S.; Jang, Y.J.; Jang, H.W.; Kim, S.Y.; Ahn, S.H. Recent advances in electrochemical, photochemical, and photoelectrochemical reduction of CO_2 to C_{2+} products. *Small* **2023**, *19*, 2205765. [CrossRef]
12. Liu, B.; Wang, T.; Wang, S.J.; Zhang, G.; Zhong, D.Z.; Yuan, T.H.; Dong, H.; Wu, B.; Gong, J.L. Back-illuminated photoelectrochemical flow cell for efficient CO_2 reduction. *Nat. Commun.* **2022**, *13*, 7111. [CrossRef]
13. Zhang, W.J.; Jin, Z.; Chen, Z.P. Rational-designed principles for electrochemical and photoelectrochemical upgrading of CO_2 to value-added chemicals. *Adv. Sci.* **2022**, *9*, 2105204. [CrossRef]
14. Wang, P.L.; Wang, S.C.; Wang, H.Q.; Wu, Z.B.; Wang, L.Z. Recent progress on photo-electrocatalytic reduction of carbon dioxide. *Part. Part. Syst. Charact.* **2018**, *35*, 1700371. [CrossRef]
15. Kumaravel, V.; Bartlett, J.; Pillai, S.C. Photoelectrochemical conversion of carbon dioxide (CO_2) into fuels and value-added products. *ACS Energy Lett.* **2020**, *5*, 486–519. [CrossRef]
16. Gyawali, S.; Tirumala, R.T.A.; Loh, H.; Andiappan, M.; Bristow, A.D. Photocarrier recombination dynamics in highly scattering Cu_2O nanocatalyst clusters. *J. Phys. Chem. C* **2024**, *125*, 2003–2011. [CrossRef] [PubMed]

17. Gyawali, S.; Tirumala, R.T.A.; Andiappan, M.; Bristow, A.D. Size- and shape-dependent charge-carrier dynamics in sub-micron cuprous oxide nanoparticles. *Front. Opt.* **2022**, JTu4A.86.

18. Liu, G.H.; Wang, K.Y.; Hoivik, N.; Jakobsen, H. Progress on free-standing and flow-through TiO_2 nanotube membranes. *Sol. Sol. Energy Mater. Sol. Cells* **2012**, *98*, 24–38. [CrossRef]

19. Schreier, M.; Luo, J.S.; Gao, P.; Moehl, T.; Mayer, M.T.; Grätzel, M. Covalent immobilization of a molecular catalyst on Cu_2O photocathodes for CO_2 reduction. *J. Am. Chem. Soc.* **2016**, *138*, 1938–1946. [CrossRef]

20. Tirumala, R.T.A.; Gyawali, S.; Wheeler, A.; Ramakrishnan, S.B.; Sooriyagoda, R.; Mohammadparast, F.; Khatri, N.; Tan, S.S.; Kalkan, A.K.; Bristow, A.D.; et al. Structure-property-performance relationships of cuprous oxide nanostructures for dielectric Mie resonance-enhanced photocatalysis. *ACS Catal.* **2022**, *12*, 7975–7985. [CrossRef]

21. Liu, J.; Xia, C.F.; Zaman, S.; Su, Y.Q.; Tan, L.; Chen, S.H. Surface plasmon assisted photoelectrochemical carbon dioxide reduction: Progress and perspectives. *J. Mater. Chem. A* **2023**, *11*, 16918–16932. [CrossRef]

22. Zhou, L.N.; Lou, M.H.; Bao, J.L.; Zhang, C.; Liu, J.G.; Martirez, J.M.P.; Tian, S.; Yuan, L.; Swearer, D.F.; Robatjazi, H.; et al. Hot carrier multiplication in plasmonic photocatalysis. *PNAS* **2021**, *118*, e2022109118. [CrossRef]

23. Huang, L.; Zaman, S.; Tian, X.L.; Wang, Z.T.; Fang, W.S.; Xia, B.Y. Advanced platinum-based oxygen reduction electrocatalysts for fuel cells. *Acc. Chem. Res.* **2021**, *54*, 311–322. [CrossRef]

24. Mohammadparast, F.; Tirumala, R.T.A.; Ramakrishnan, S.B.; Dadgar, A.P.; Andiappan, M. Operando UV-Vis spectroscopy as potential in-line PAT system for size determination of functioning metal nanocatalysts. *Chem. Eng. Sci.* **2020**, *225*, 115821. [CrossRef]

25. Du, W.; Li, M.; Liu, Q.; Chen, R. Improving the electrocatalytic CO_2 reduction performance of Bi catalysts for formic acid production via size control, morphology regulation and carbon complexation. *New J. Chem.* **2024**, *48*, 6000. [CrossRef]

26. Cui, Y.J.; Cheng, Y.H.; Yang, C.L.; Su, Y.S.; Yao, D.F.; Liufu, B.P.; Li, J.L.; Fang, Y.W.; Liu, S.Y.; Zhong, Z.Y. High-performance electrocatalytic CO_2 reduction for CO generation using hydrophobic porous carbon supported Au. *ACS Sustain. Chem. Eng.* **2023**, *11*, 11229–11238. [CrossRef]

27. Wang, T.; Wang, Y.; Li, Y.; Li, C. The origins of catalyst selectivity for the electrochemical conversion of carbon dioxide to methanol. *Nano Res.* **2024**, *17*, 5–17. [CrossRef]

28. Lal, D.; Konnur, T.; Verma, A.M.; Shaneeth, M.; Rajan, A.G. Unraveling low overpotential pathways for electrochemical CO_2 reduction to CH_4 on pure and doped MoS_2 edges. *Ind. Eng. Chem. Res.* **2023**, *62*, 21191–21207. [CrossRef]

29. Liu, Y.M.; Chen, S.; Quan, X.; Yu, H.T. Efficient electrochemical reduction of carbon dioxide to acetate on nitrogen-doped nanodiamond. *J. Am. Chem. Soc.* **2015**, *137*, 11631–11636. [CrossRef] [PubMed]

30. Peng, C.; Luo, G.; Zhang, J.B.; Chen, M.H.; Wang, Z.Q.; Sham, T.K.; Zhang, L.J.; Li, Y.F.; Zheng, G.F. Double sulfur vacancies by lithium tuning enhance CO_2 electroreduction to n-propanol. *Nat. Commun.* **2021**, *12*, 1580. [CrossRef] [PubMed]

31. Xue, S.S.; Liang, X.Y.; Zhang, Q.; Ren, X.F.; Gao, L.G.; Ma, T.L.; Liu, A.M.; Pasti, I.A. Density functional theory study of CuAg bimetal electrocatalyst for CO_2RR to produce CH_3OH. *Catalysts* **2024**, *14*, 7. [CrossRef]

32. Zhang, Z.; Bian, L.; Tian, H.; Liu, Y.; Bando, Y.; Yamauchi, Y.; Wang, Z.-L. Tailoring the surface and interface structures of copper-based catalysts for electrochemical reduction of CO_2 to ethylene and ethanol. *Small* **2022**, *18*, 2107450. [CrossRef]

33. Borovinskaya, E.S.; Trebbin, S.; Alscher, F.; Breitkopf, C. Synthesis, modification, and characterization of $CuO/ZnO/ZrO_2$ mixed metal oxide catalysts for CO_2/H_2 conversion. *Catalysts* **2019**, *9*, 1037. [CrossRef]

34. Gao, D.; Arán-Ais, R.M.; Jeon, H.S.; Cuenya, B.R. Rational catalyst and electrolyte design for CO_2 electroreduction towards multicarbon products. *Nat. Catal.* **2019**, *2*, 198–210. [CrossRef]

35. Song, Z.; Wang, X.; Ren, Z.; Fu, H. Relationships between structural design and synthesis engineering of Cu-based catalysts for CO_2 to C_2 electroreduction. *Chem. Eng. J.* **2024**, *479*, 147606. [CrossRef]

36. Wu, Z.-Z.; Zhang, X.-L.; Niu, Z.-Z.; Gao, F.-Y.; Yang, P.-P.; Chi, L.-P.; Shi, L.; Wei, W.-S.; Liu, R.; Chen, Z.; et al. Identification of Cu(100)/Cu(111) interfaces as superior active sites for CO dimerization during CO_2 electroreduction. *J. Am. Chem. Soc.* **2022**, *144*, 259–269. [CrossRef]

37. Jiang, K.; Sandberg, R.B.; Akey, A.J.; Liu, X.; Bell, D.C.; Nørskov, J.K.; Chan, K.; Wang, H. Metal ion cycling of Cu foil for selective C–C coupling in electrochemical CO_2 reduction. *Nat. Catal.* **2018**, *1*, 111–119. [CrossRef]

38. Guo, S.Y.; Liu, Y.C.; Murphy, E.; Ly, A.; Xu, M.J.; Matanovic, I.; Pan, X.Q.; Atanassov, P. Robust palladium hydride catalyst for electrocatalytic formate formation with high CO tolerance. *Appl. Catal. B* **2022**, *16*, 121659. [CrossRef]

39. Liu, S.; Zhang, B.S.; Zhang, L.H.; Sun, J. Rational design strategies of Cu-based electrocatalysts for CO_2 electroreduction to C_2 products. *J. Energy Chem.* **2022**, *71*, 63–82. [CrossRef]

40. Schouten, K.J.P.; Gallent, E.P.; Koper, M.T.M. Structure sensitivity of the electrochemical reduction of carbon monoxide on copper single crystals. *ACS Catal.* **2013**, *3*, 1292–1295. [CrossRef]

41. Schouten, K.J.P.; Kwon, Y.; van der Ham, C.J.M.; Qin, Z.; Koper, M.T.M. A new mechanism for the selectivity to C_1 and C_2 species in the electrochemical reduction of carbon dioxide on copper electrodes. *Chem. Sci.* **2011**, *2*, 1902. [CrossRef]

42. Karapinar, D.; Creissen, C.E.; de la Cruz, J.G.R.; Schreiber, M.W.; Fontecave, M. Electrochemical CO_2 reduction to ethanol with copper-based catalysts. *ACS Energy Lett.* **2021**, *6*, 694–706. [CrossRef]

43. Hori, Y.; Wakebe, H.; Tsukamoto, T.; Koga, O. Adsorption of CO accompanied with simultaneous charge transfer on copper single crystal electrodes related with electrochemical reduction of CO_2 to hydrocarbons. *Surf. Sci.* **1995**, *335*, 258–263. [CrossRef]

44. Hori, Y.; Takahashi, I.; Koga, O.; Hoshi, N. Electrochemical reduction of carbon dioxide at various series of copper single crystal electrodes. *J. Mol. Catal. A Chem.* **2003**, *199*, 39–47. [CrossRef]

45. Gattrell, M.; Gupta, N.; Co, A. A review of the aqueous electrochemical reduction of CO_2 to hydrocarbons at copper. *J. Electroanal. Chem.* **2006**, *594*, 1–19. [CrossRef]

46. Perez-Gallent, E.; Figueiredo, M.C.; Calle-Vallejo, F.; Koper, M.T.M. Spectroscopic observation of a hydrogenated CO dimer intermediate during CO reduction on Cu(100) electrodes. *Angew. Chem. Int. Ed.* **2017**, *56*, 3621–3624. [CrossRef]

47. Ou, L.H.; He, Z.X.; Yang, H.; Chen, Y.D. Theoretical insights into potential-dependent C-C bond formation mechanisms during CO_2 electroreduction into C_2 products on Cu(100) at simulated electrochemical interfaces. *ACS Omega* **2021**, *6*, 17839–17847. [CrossRef]

48. Zhang, R.; Sun, X.; Wang, B. Insight into the preference mechanism of CH_x(x = 1–3) and C-C chain formation involved in C_2 oxygenate formation from syngas on the Cu(110) surface. *J. Phys. Chem. C* **2013**, *117*, 6594–6606. [CrossRef]

49. Kuo, T.-C.; Chou, J.-W.; Shen, M.-H.; Hong, Z.-S.; Chao, T.-H.; Lu, Q.; Cheng, M.-J. First-principles study of C-C coupling pathways for CO_2 electrochemical reduction catalyzed by Cu(110). *J. Phys. Chem. C* **2021**, *125*, 2464–2476. [CrossRef]

50. Bagger, A.; Ju, W.; Varela, A.S.; Strasser, P.; Rossmeisl, J. Electrochemical CO_2 reduction: Classifying Cu facets. *ACS Catal.* **2019**, *9*, 7894–7899. [CrossRef]

51. Takahashi, I.; Koga, O.; Hoshi, N.; Hori, Y. Electrochemical reduction of CO_2 at copper single crystal Cu(S)-[n(111)×(111)] and Cu(S)-[n(110)×(100)] electrodes. *J. Electroanal. Chem.* **2002**, *533*, 135–143. [CrossRef]

52. Nørskov, J.K.; Bligaard, T.; Logadottir, A.; Kitchin, J.; Chen, J.G.; Pandelov, S.; Stimming, U. Trends in the exchange current for hydrogen evolution. *J. Electrochem. Soc.* **2005**, *152*, J23–J26. [CrossRef]

53. Luo, W.J.; Nie, X.W.; Janik, M.J.; Asthagiri, A. Facet dependence of CO_2 reduction paths on Cu electrodes. *ACS Catal.* **2016**, *6*, 219–229. [CrossRef]

54. Jo, D.Y.; Ham, H.C.; Lee, K.Y. Facet-dependent electrocatalysis in the HCOOH synthesis from CO_2 reduction on Cu catalyst: A density functional theory study. *Appl. Surf. Sci.* **2020**, *527*, 146857. [CrossRef]

55. van Rensburg, W.J.; Petersen, M.A.; Datt, M.S.; van den Berg, J.A.; van Helden, P. On the kinetic interpretation of DFT-derived energy profiles: Cu-catalyzed methanol synthesis. *Catal. Lett.* **2015**, *145*, 559–568. [CrossRef]

56. Liu, W.; Zhai, P.B.; Li, A.W.; Wei, B.; Si, K.P.; Wei, Y.; Wang, X.G.; Zhu, G.D.; Chen, Q.; Gu, X.K.; et al. Electrochemical CO_2 reduction to ethylene by ultrathin CuO nanoplate arrays. *Nat. Commun.* **2022**, *13*, 1877. [CrossRef]

57. Xue, Q.; Qi, X.; Li, K.; Zeng, Y.; Xu, F.; Zhang, K.; Yang, T.; Qi, X.; Jiang, J. DFT study of CO_2 reduction reaction to CH_3OH on low-index Cu surfaces. *Catalysts* **2023**, *13*, 722. [CrossRef]

58. Shin, D.Y.; Jo, J.H.; Lee, J.Y.; Lim, D.H. Understanding mechanisms of carbon dioxide conversion into methane for designing enhanced catalysts from first-principles. *Comput. Theor. Chem.* **2016**, *1083*, 31–37. [CrossRef]

59. Montoya, J.H.; Shi, C.; Chan, K.; Norskov, J.K. Theoretical insights into a CO dimerization mechanism in CO_2 electroreduction. *J. Phys. Chem. Lett.* **2015**, *6*, 2032–2037. [CrossRef]

60. Guo, S.Y.; Liu, Y.C.; Huang, Y.; Wang, H.S.; Murphy, E.; Delafontaine, L.; Chen, J.L.; Zenyuk, I.V.; Atanassov, P. Promoting electrolysis of carbon monoxide toward acetate and 1-propanol in flow electrolyzer. *ACS Energy Lett.* **2023**, *8*, 935–942. [CrossRef]

61. Jouny, M.; Hutchings, G.S.; Jiao, F. Carbon monoxide electroreduction as an emerging platform for carbon utilization. *Nat. Catal.* **2019**, *2*, 1062–1070. [CrossRef]

62. Karamad, M.; Hansen, H.A.; Rossmeisl, J.; Nørskov, J.K. Mechanistic pathway in the electrochemical reduction of CO_2 on RuO_2. *ACS Catal.* **2015**, *5*, 4075–4081. [CrossRef]

63. Kuhl, K.P.; Cave, E.R.; Abram, D.N.; Jaramillo, T.F. New insights into the electrochemical reduction of carbon dioxide on metallic copper surfaces. *Energy Environ. Sci.* **2012**, *5*, 7050. [CrossRef]

64. Kresse, G.; Hafner, J. *Ab initio* molecular dynamics for liquid metals. *Phys. Rev. B* **1993**, *47*, 558. [CrossRef] [PubMed]

65. Kresse, G.; Furthmuüller, J. Efficient iterative schemes for ab initio total-energy calculations using a plane-wave basis set. *Phys. Rev. B* **1996**, *54*, 11169. [CrossRef] [PubMed]

66. Perdew, J.P.; Burke, K.; Ernzerhof, M. Generalized gradient approximation made simple. *Phys. Rev. Lett.* **1996**, *77*, 3865. [CrossRef] [PubMed]

67. Yang, Y.; Wang, L.; Zhang, Z.; Cui, P. Prediction of a kinetic pathway for fabricating the narrowest zigzag graphene nanoribbons on Cu(111). *J. Phys. Chem. C* **2021**, *125*, 21933–21942. [CrossRef]

68. Mo, Y.; Zhu, W.; Kaxiras, E.; Zhang, Z. Electronic nature of step-edge barriers against adatom descent on transition-metal surfaces. *Phys. Rev. Lett.* **2018**, *101*, 216101. [CrossRef] [PubMed]

69. Phatak, A.A.; Delgass, W.N.; Ribeiro, F.H.; Schneider, W.F. Density functional theory comparison of water dissociation steps on Cu, Au, Ni, Pd, and Pt. *J. Phys. Chem. C* **2009**, *113*, 7269–7276. [CrossRef]

70. Grimme, S.; Antony, J.; Ehrlich, S.; Krieg, H. A consistent and accurate ab initio parametrization of density functional dispersion correction (DFT-D) for the 94 elements H-Pu. *J. Chem. Phys.* **2010**, *132*, 154104. [CrossRef]

71. Li, Z.Y.; Li, N.; Wang, N.; Zhou, B.; Yin, P.; Song, B.Y.; Yu, J.; Yang, Y.S. Mechanism investigations on water gas shift reaction over Cu(111), Cu(100), and Cu(211) surfaces. *ACS Omega* **2022**, *7*, 3514–3521. [CrossRef] [PubMed]

72. Jiang, J.C.; Chen, J.C.; Zhao, M.D.; Yu, Q.; Wang, Y.G.; Li, J. Rational design of copper-based single-atom alloy catalysts for electrochemical CO_2 reduction. *Nano Res.* **2022**, *15*, 7116–7123. [CrossRef]

73. Henkelman, G.; Uberuaga, B.P.; Jónsson, H. Improved tangent estimate in the nudged elastic band method for finding minimum energy paths and saddle points. *J. Chem. Phys.* **2000**, *113*, 9901. [CrossRef]

74. Nie, X.W.; Jiang, X.; Wang, H.Z.; Luo, W.J.; Janik, M.J.; Chen, Y.G.; Guo, X.W.; Song, C.S. Mechanistic understanding of alloy effect and water promotion for Pd-Cu bimetallic catalysts in CO_2 hydrogenation to methanol. *ACS Catal.* **2018**, *8*, 4873–4892. [CrossRef]

75. Bai, H.; Ma, M.M.; Bai, B.; Zuo, J.P.; Cao, H.J.; Zhang, L.; Zhang, Q.F.; Vinokurov, V.A.; Huang, W. The active site of syngas conversion into ethanol over $Cu/ZnO/Al_2O_3$ ternary catalysts in slurry bed. *J. Catal.* **2019**, *380*, 68–82. [CrossRef]

76. Durand, W.J.; Peterson, A.A.; Studt, F.; Abild-Pedersen, F.; Nørskov, J.K. Structure effects on the energetics of the electrochemical reduction of CO_2 by copper surfaces. *Surf. Sci.* **2011**, *605*, 1354–1359. [CrossRef]

77. Vegge, T.; Rasmussen, T.; Leffers, T.; Pedersen, O.B.; Jacobsen, K.W. Atomistic simulations of cross-slip of jogged screw dislocations in copper. *Philos. Mag. Lett.* **2001**, *81*, 137–144. [CrossRef]

78. Dong, H.L.; Li, Y.Y.; Jiang, D.E. First-principles insight into electrocatalytic reduction of CO_2 to CH_4 on a copper nanoparticle. *J. Phys. Chem. C* **2018**, *122*, 11392–11398. [CrossRef]

79. Maulana, A.L.; Putra, R.I.D.; Saputro, A.G.; Agusta, M.K.; Nugrahaab; Dipojono, H.K. DFT and microkinetic investigation of methanol synthesis via CO_2 hydrogenation on Ni(111)-based surfaces. *Phys. Chem. Chem. Phys.* **2019**, *21*, 20276. [CrossRef]

80. Reichenbach, T.; Mondal, K.; Jäger, M.; Vent-Schmidt, T.; Himmel, D.; Dybbert, V.; Bruix, A.; Krossing, I.; Walter, M.; Moseler, M. Ab initio study of CO_2 hydrogenation mechanisms on inverse ZnO/Cu catalysts. *J. Catal.* **2018**, *360*, 168–174. [CrossRef]

81. Chang, C.C.; Ku, M.S. Role of high-index facet Cu(711) surface in controlling the C_2 selectivity for CO_2 reduction reaction—A DFT study. *J. Phys. Chem. C* **2021**, *125*, 10919–10925. [CrossRef]

82. Zhao, Y.; Zhang, X.G.; Bodappa, N.; Yang, W.M.; Liang, Q.; Radjenovica, P.M.; Wang, Y.H.; Zhang, Y.J.; Dong, J.C.; Tian, Z.Q.; et al. Elucidating electrochemical CO_2 reduction reaction processes on Cu(hkl) single-crystal surfaces by in situ Raman spectroscopy. *Energy Environ. Sci.* **2022**, *15*, 3968–3977. [CrossRef]

83. Gao, S.T.; Xiang, S.Q.; Shi, J.L.; Zhang, W.; Zhao, L.B. Theoretical understanding of the electrochemical reaction barrier: A kinetic study of CO_2 reduction reaction on copper electrodes. *Phys. Chem. Chem. Phys.* **2020**, *22*, 9607–9615. [CrossRef] [PubMed]

84. Grabow, L.C.; Mavrikakis, M. Mechanism of Methanol Synthesis on Cu through CO_2 and CO Hydrogenation. *ACS Catal.* **2011**, *1*, 365–384. [CrossRef]

85. Wang, Y.X.; Wang, G.C. A Systematic Theoretical study of water gas shift reaction on Cu(111) and Cu(110): Potassium effect. *ACS Catal.* **2019**, *9*, 2261–2274. [CrossRef]

86. Mandal, S.C.; Rawat, K.S.; Garg, P.; Pathak, B. Hexagonal Cu(111) Monolayers for selective CO_2 hydrogenation to CH_3OH: Insights from density functional theory. *ACS Appl. Nano Mater.* **2020**, *2*, 7686–7695. [CrossRef]

87. Chen, Z.; Ma, Z.; Fan, G.; Li, F. Critical role of Cu nanoparticle-loaded Cu(100) surface structures on structured copper-based catalysts in boosting ethanol generation in CO_2 electroreduction. *ACS Appl. Mater. Interfaces* **2024**, *16*, 35143–35154. [CrossRef]